

Published in final edited form as:

Neuroimage. 2010 April 1; 50(2): 456–464. doi:10.1016/j.neuroimage.2009.12.107.

***In vivo* MRI of neural cell migration dynamics in the mouse brain**

Brian J. Nieman^{a,b,1}, Jeffrey Y. Shyu^a, Joe J. Rodriguez^a, A. Denise Garcia^d, Alexandra L. Joyner^d, and Daniel H. Turnbull^{a,b,c,*}

^aKimmel Center for Biology and Medicine at the Skirball Institute of Biomolecular Medicine, New York University School of Medicine, NY, USA

^bDepartment Radiology, New York University School of Medicine, NY, USA

^cDepartment Pathology, New York University School of Medicine, NY, USA

^dDevelopmental Biology Program, Sloan-Kettering Institute, NY, USA

Abstract

Multipotent neuroblasts (NBs) are produced throughout life by neural stem cells in the forebrain subventricular zone (SVZ), and are able to travel long distances to the olfactory bulb. On arrival in the bulb, migrating NBs normally replace olfactory neurons, raising interest in their potential for novel cell replacement therapies in various disease conditions. An understanding of the migratory capabilities of NBs is therefore important, but as yet quantitative *in vivo* measurement of cell migration has not been possible. In this study, targeted intracerebral injections of iron-oxide particles to the mouse SVZ were used to label resident NBs *in situ*, and their migration was tracked noninvasively over time with magnetic resonance imaging (MRI). Quantitative intensity metrics were employed to identify labeled cells and to show that cells are able to travel at speeds up to 100 $\mu\text{m/h}$ en route to the olfactory bulb, but that distribution through the olfactory bulb occurs at a much slower rate. In addition, comparison of histological and MRI measures of iron-oxide particle distribution were in excellent agreement. Immunohistochemistry analysis 1–3 weeks after labeling revealed that the majority of labeled cells in the olfactory bulb were immature neurons, although iron-oxide particles were also found in astrocytes and microglia. This work indicates that dynamic measurements of endogenous cell migration can be made with MRI and represents the first *in vivo* measurement of NB migration rates. The use of MRI in future studies tracking endogenous NB cells will permit a more complete evaluation of their role during homeostasis at various developmental stages and during disease progression.

Keywords

Magnetic resonance imaging; Micron-sized particles of iron-oxide, MPIO; Subventricular zone, SVZ; Neural stem cells; Neuroblast; Cell migration

Introduction

Sustained production of neuroblasts (NBs) occurs throughout adulthood in the mammalian central nervous system (CNS) in two established cell niches, the subgranular zone, and the subventricular zone (SVZ) (Bayer et al., 1982; Corotto et al., 1993). NBs produced in the SVZ

© 2009 Elsevier Inc. All rights reserved.

*Corresponding author. Skirball Institute of Biomolecular Medicine, 5th Floor, Labs 6-7, 540 First Avenue, NY 10016, USA. Daniel.Turnbull@med.nyu.edu (D.H. Turnbull).

¹Current address: Mouse Imaging Centre, Hospital for Sick Children and Toronto Centre for Phenogenomics, Toronto ON, Canada.

are particularly critical for neuronal homeostasis in the olfactory bulb (OB), where they are required to replenish various types of interneurons throughout adulthood (Lledo et al., 2008; Lois and Alvarez-Buylla, 1994). These cells migrate from their origin in the SVZ rostrally, and then along a sharply defined pathway known as the rostral migratory stream (RMS), which bridges the large distance between the SVZ and the OB. Interestingly, damage to the brain through acute injury or chronic disease has been shown to alter NB activities. Increased rates of proliferation have been detected following ischemia (Arvidsson et al., 2002; Thored et al., 2006), demyelination (Nait-Oumesmar et al., 1999), or excitotoxic injury (Tattersfield et al., 2004) and NBs have been shown to migrate from the SVZ to sites of brain damage where they can promote some functional recovery, especially after treatment with defined growth factors (Cooper and Isacson, 2004; Fallon et al., 2000; Kolb et al., 2007). This introduces the possibility that NBs from the SVZ could participate in CNS repair in regions of the brain other than the OB. Enhancement of such an endogenous repair response, for example with administered growth factors, would be an exciting therapeutic possibility for many disease conditions.

Clearly, the dynamics of endogenous NB migration—including the speed, spatial distribution and timing—relative to disease progression are of critical importance in assessing any such therapeutic potential. Various methods have been used to estimate the normal rate of NB migration from or through the SVZ. In the rat neonate, retroviral labeling and counting of cells in serial sections were used to estimate an average RMS speed of $\sim 23 \mu\text{m/h}$ (Luskin and Boone, 1994). *In vitro* measurements in a cell culture system suggested much faster speeds of $120 \mu\text{m/h}$ (Wichterle et al., 1997). More recently, time-lapse analyses in mouse brain slice explants have yielded estimated speeds of $\sim 50 \mu\text{m/h}$ in the adult SVZ (Bolteus and Bordey, 2004) and $\sim 89 \mu\text{m/h}$ in the neonatal RMS (Hirota et al., 2007). The slice explants method is feasible only because the RMS, although curved in profile, resides largely in a sagittal plane. More complex three-dimensional patterns of migration or cellular distribution—which may result after disease or injury—cannot be assessed in the same fashion. Methods of noninvasively and longitudinally detecting NB distribution would permit more detailed measurements of RMS migration properties and importantly, permit characterization of the more complex movement patterns associated with possible disease response.

In situ labeling of endogenous SVZ cells in the adult rat has been demonstrated by injections of micron-sized particles of iron-oxide (MPIOs) into the lateral ventricle with subsequent detection by magnetic resonance imaging (MRI) (Shapiro et al., 2006). MRI provides the distinct advantage of providing inherently three-dimensional data with the capability of longitudinal temporal evaluation. However, the migration rate of MPIO-labeled cells has not been evaluated with longitudinal studies in individual animals, nor have strictly quantitative image intensity metrics been used to describe the MR-detected distributions of labeled cells.

In this study, the potential of mouse MRI was investigated for quantitative analysis of NB migration in the RMS, characterization of NB distribution in the OB, and evaluation of labeled cell types at two time points. For this purpose, we introduced a modified MPIO-labeling protocol in which MPIO injections are targeted directly to the anterior SVZ and then followed by serial MR imaging of individual mice. Importantly, these studies serve to: (1) verify the feasibility of labeling mouse NBs *in situ* with small-volume, SVZ-targeted MPIO injections; (2) quantify normal NB migration rates in the RMS; (3) characterize NB distribution through the OB over time; and (4) evaluate migrating MPIO-labeled cell types.

Materials and methods

Animals

All animal studies described in this report were approved by the Institutional Animal Care and Use Committee at New York University School of Medicine. Studies were performed using 6–10 week old, female ICR mice (Taconic Farms, Hudson, NY).

Surgical injections

For injection of MPIOs, mice were anesthetized using isoflurane and placed in a stereotaxic frame. The head was shaved and a ~1 cm incision was made to expose the skull. Using a microdrill, a 1–2 mm hole was produced to allow an injection into the anterior portion of the SVZ (stereotaxic coordinates 0.7–0.9 mm lateral to bregma, 1.1–1.3 mm rostral to bregma and 2.4–2.6 mm deep from the pial surface). All injections were performed with glass microcapillary tubes (0.5 mm ID, 1.0 mm OD, 10 cm length, Sutter Instruments, Novato, CA), pulled and cut to produce a 100 μm diameter needle tip and mounted on a microinjector (Narishige International, East Meadow, NY). MPIO solution (50 nl, $\sim 1.5 \times 10^6$ particles) was injected as provided by the manufacturer (encapsulated, fluorescent, magnetic beads, nominal 1.63 μm diameter, 520/480 nm excitation/emission, Bangs Laboratories, Inc, Fishers, IN). Following surgery, the skin over the skull was sutured closed and animals were placed in separate, heated cages and monitored until fully recovered.

Magnetic resonance imaging

All imaging experiments were performed on a 7T 200-mm bore Magnex magnet equipped with a Bruker Biospec Avance II console (Bruker Biospin MRI, Ettlingen, Germany) and actively shielded gradients (BGA9S, Bruker Biospin MRI). Images were collected using a quadrature, transmit/receive Litzcage volume coil (25 mm inner diameter, Doty Scientific, Columbia, SC, USA). For visualization of MPIO distribution, a multiple gradient-echo image acquisition sequence was employed (TR = 40 ms, TE = 4.0, 8.3 ms, 12° excitation angle and 8 repeats). Image dimensions included a field-of-view of 25.6 \times 19.2 \times 12.8 mm and matrix size 256 \times 192 \times 128 to yield 100 μm isotropic voxels in an imaging time of 2 h, 12 min. Image reconstruction with retrospective self-gating was used to minimize artifact due to respiration and motion as described previously (Nieman et al., 2009). A magnitude image was generated for each echo and then the two images were averaged to yield a single image for subsequent analysis. The averaged image provided ~30% higher signal-to-noise and contrast-to-noise ratio than either single image, while retaining a short echo-time image for clearer visualization of the injection site. Prior to imaging, animals were prepared in an induction chamber with 4–5% isoflurane in compressed air and then transferred to the imaging holder and coil assembly where they were maintained under anesthesia with 1.0–1.5% isoflurane.

Image analyses

Labeled image voxels were isolated by statistically testing for hypointense voxels (Fig. 1). Images were first registered together into a common space to align ipsilateral voxels across all images and subsequently to align the contralateral voxels as well. This process, including each of the steps described below, was performed separately for analyses of RMS migration rates and OB distribution. For the migration rate analyses, image time points included Days 0 (~2 h post-injection), 1 and 2. The OB distribution analyses included images from Days 0–1 (comprised of images collected 3 to 24 h post-injection), 4, 7 and 21. In each case, the image processing began by positional alignment and intensity normalization of all images. The latter included correction for nonuniformity (Sled et al., 1998) and histogram normalization. All images were then registered together to generate an unbiased space into which all images were resampled. This process has been described in several previous publications (Kovacevic et al.,

2005; Lerch et al., 2008; Nieman et al., 2006; Woods et al., 1998a,b). The unbiased space was defined through a process of pairwise linear registrations and then refined through an iterative nonlinear registration of the individual images. For these analyses, the region of the MPIO injection was excluded from the registration process with a mask and the final nonlinear registration step was limited to a coarse resolution (300 μm). This permitted alignment of the olfactory bulbs without fine adjustment of isolated hypointense voxels, which appear somewhat stochastically through the OB at late stages. All registrations were performed using software tools from the Montreal Neurological Institute (Collins et al., 1994).

With images registered together, individual voxels were determined to be hypointense—and therefore “labeled”—by comparison of the intensity value in the ipsilateral side to the corresponding values in the equivalent contralateral voxel. This comparison was performed for each voxel in the forebrain and OB. To isolate the relevant voxel on the contralateral side of the brain, all images were mirrored left to right and then registered to the common space. Subsequently, the set of contralateral intensity values at the voxel of interest and from all acquired images was used as reference values to assign a p -value to each ipsilateral voxel using a one-sided Student’s t -test. Statistical thresholds were then applied using a false discovery rate (FDR, $q = 0.05$) to correct for multiple comparisons (Benjamini and Hochberg, 1995). For visualization of the distribution of particles, thresholded binary maps of hypointense voxels were overlaid on the average images.

In order to facilitate visualization of the RMS in three dimensions, two image planes were generated for viewing. The first image plane was a conventional parasagittal plane running through the center of the OB ipsilateral to the injection site. The second plane was a curvilinear plane perpendicular to the parasagittal plane and running along the curved path of the RMS, enabling clear visualization of the lateral distribution of MPIOs about the RMS and in the OB. This second plane was generated by manually identifying points on the RMS path in the average images and then using tricubic interpolation to generate signal intensities at equidistant sites on the curved path.

To estimate the speed of MPIO movement from MR images, the location of hypointense voxels was compared on consecutive days in images from individual mice. The distance between the detected voxels furthest along the RMS was computed along the curved path of the RMS. An average was determined for the maximum speed between Days 0 and 1 and between Days 1 and 2 by calculating the speeds in each mouse and then averaging the results. This method tended to detect the fastest migrating cells and therefore produced an average of the maximum RMS migration rate.

Histological analyses

On Days 2, 7 or 21 after MPIO injection, selected mice were prepared for histological analysis. For this purpose, mice received an intraperitoneal injection of nembutal (400 mg/kg), and were perfusion fixed through the left ventricle with 4 °C, 4% paraformaldehyde (PFA, Sigma-Aldrich, St. Louis, MO). After extraction from the skull and post-fixation (overnight in 4 °C, 4% PFA), brains were cryoprotected in 30% sucrose in phosphate buffered saline, mounted in embedding compound (Tissue-Tek OCT, Sakura Finetek USA Inc., Torrance, CA) and frozen into blocks. Sections were cut serially at 20 μm thickness on a cryostat (CM3050S, Leica Microsystems, Bannockburn, IL).

The Day 2 specimens were used to verify the MR detected particle distribution with histological counts of the distribution. In cryostat sections, the rostral–caudal distribution of particles was characterized by counting particles prior to any staining. Particles were visualized using a fluorescence dissection scope (Leica MZ16F, Leica Microsystems) and the total particle count in each section was recorded. Where sections were damaged or missing, a count was assigned

based on the averages of the nearest 5 available sections. In this manner, a complete rostral–caudal particle count distribution was determined. In order to compare with MRI results (in which the voxel size was 100 μm), the counts from every five consecutive (20 μm) slices were summed to estimate the expected total particle count in serial 100 μm thick sections. A comparable metric was generated from the MRI images by counting the MRI hypointense voxels from planes running in the same rostral–caudal dimension. The image voxel and particle count distributions were then aligned by maximizing the correlation between the two distributions. By virtue of the registration of separate MR images, separate histological particle count distributions were also brought to a common space and, therefore, an average particle count distribution based on the histological sections was calculated and compared to the average hypointense voxel counts by MRI. For visualization of the histology sections, the histogram of the resultant images was manipulated to highlight the auto-fluorescent signal from the tissue, thus putting the much brighter MPIO fluorescence into an anatomical context.

Immunohistochemistry

Selected mice were injected with bromodeoxyuridine (BrdU, 100 mg/kg, Sigma) once per day for 3 days immediately following MPIO injection. BrdU is incorporated into cells during cell division, and marks dividing cells in the SVZ. Sections from these mice were visualized after staining for BrdU and for Nissl. Evaluation of these sections permitted visualization of the particle distribution in the SVZ at the ventricles and qualitative comparison of MPIO and BrdU distribution.

Serial sections were stained at different time points to identify which cell types contained MPIOs. For Day 2 images, Glial fibrillary acidic protein (GFAP, an astrocyte marker) was detected using a mouse anti-GFAP primary antibody (Chemicon, Millipore Corp., Billerica, MA). Likewise, doublecortin (Dcx, marker of migrating neuroblasts) was detected with goat anti-Dcx (Santa Cruz Biotechnology, Santa Cruz, CA). At later time points, staining was also performed with primary antibodies for Class III β -tubulin (Tuj1, immature neuronal marker) (Covance, Inc., Princeton, NJ) and Ionized calcium binding adaptor molecule 1 (Iba1, microglial marker) (Wako Chemicals, Inc., Richmond, VA). All immunostaining used IgG Cy3 secondary antibodies (Jackson ImmunoResearch Laboratories Inc., West Grove, PA), following protocols provided by the manufacturers.

Following staining, three independent readers scored each section for labeled cells by counting the total number of MPIOs per section and the subset localized within stained cells. Cell localization was determined by inspection based upon the proximity of MPIOs to stained cells. An average reader count for each section was computed and then the total for all sections was tabulated. Cell types were assessed at both Day 2 and Day 21. All counts included at least 3 different mice and a total of at least 500 and 85 MPIO particles per stain type for Day 2 and Day 21, respectively.

Results

SVZ-targeted MPIO injections resulted in rapid MPIO migration in the RMS

Stereotaxic injection of MPIO particles in the anterior region of the SVZ resulted in hypointense artifacts at the site of injection on T_2^* -weighted images immediately after surgery. Injections frequently showed evidence of MPIOs in the lateral ventricle adjacent to the injection site, a result that could not be completely eliminated by adjustment of stereotaxic coordinates due to the small size of the SVZ and its close proximity to the ventricle. Follow-up images 24 h postinjection showed significant hypointense regions extending along the putative path of the RMS and away from the injection site artifact, suggesting transport of the MPIOs. After initial experimentation with the methodology, this labeling was successful in approximately

70% of surgeries. For analyses, hypointense voxels were determined by statistical comparison to intensity values in the contralateral voxel. The most distal MPIO-labeled voxels were detected, and the distance traveled between Days 0 and 1 and between Days 1 and 2 was computed. From these data, an average maximum migration speed of 102 $\mu\text{m}/\text{h}$ was estimated in the RMS (Days 0–1), while the speed slowed significantly in the initial, caudal part of the olfactory bulb (49 $\mu\text{m}/\text{h}$) between Days 1 and 2 (Fig. 2).

MPIO-labeled cells distributed slowly through the OB

MRI at later time points revealed a slow distribution of MPIOs through the olfactory bulb (Fig. 3). By Day 4, the particles were found throughout much of the medial region of the olfactory bulb, while relatively smaller changes in distribution were observed through Days 7 and 21. Throughout the 3-week observation period, the distribution of the particles in the olfactory bulb was predominantly parasagittal in orientation, with more limited movement of particles laterally (Fig. 3).

Hypointense image voxels accurately mapped the MPIO spatial distribution

On Day 2, detailed comparisons were made between the distribution of MPIOs as assessed by MRI, and the distribution determined by traditional histological methods (Fig. 4). Good qualitative agreement was observed between MRI and matched histological sections (Fig. 4a). Plots of the average particle count and average voxel count as a function of position showed very similar distribution profiles (Fig. 4b). Furthermore, a direct comparison of counts at each position showed that the average voxel count and average particle count were highly correlated (Fig. 4c).

SVZ-targeted MPIO injections labeled astrocytes and migrating neuroblasts

The site of injection in the anterior SVZ was verified on MR images and was also analyzed using histological sections. Histological examination 7 days after injection showed very limited MPIO presence in the more posterior regions of the SVZ (Fig. 5a), even though MPIO particles frequently leaked into the ventricle. Accumulation of MPIOs was most evident in the targeted anterior region of the SVZ (Figs. 5b, c). A majority of the MPIOs remained at or near the injection site, with isolated particles distributed throughout the regions of the RMS and OB (Figs. 5d, e). When BrdU was administered following MPIO injection, the distribution pattern of the MPIOs qualitatively matched that of BrdU positive cells, with small clusters of MPIO and BrdU distributed throughout the RMS and more widely dispersed through the medial region of the OB. Precise colocalization was infrequent and the number of MPIOs was approximately 15% of the number of BrdU-labeled cells, suggesting that these experiments did not label precisely the same cells or cell populations.

We evaluated labeled cells on Day 2 and Day 21 by immunohistochemistry in sections from the RMS and OB in the aim of detecting labeled cell type (Fig. 6, Fig. 7). On Day 2, MPIO-labeled cells were distributed largely in astrocytes and migrating NBs, which accounted for 90% of labeled cells (62% and 28% for Dcx and GFAP, respectively). Scoring the sections separately in the RMS and OB did not reveal any significant differences in the relative proportion of labeled cells in these regions.

We further evaluated MPIO-labeled cell types on Day 21 (Fig. 7). Migrating NB, marked by Dcx, and astrocytes, marked by GFAP, continued to represent a large fraction of labeled cells, although the number of labeled Dcx+ cells decreased marginally (to 50%). Immunostaining with Tuj1, a marker expected to show significant overlap with Dcx, verified the large fraction of immature neuronal cells. Notably at Day 21, a large percentage of cells (35%) was also found in Iba1+ cells, perhaps indicating cell death followed by phagocytosis of MPIO particles in microglia.

Discussion

In this paper, we presented the first detailed longitudinal measurements of the migration characteristics of NB progenitor cells originating in the SVZ of the mouse brain. These results demonstrate that at least some NBs are capable of migrating *in vivo* at 100 $\mu\text{m}/\text{h}$ or more. This is consistent with some other reported estimates (Hirota et al., 2007), and represents the first longitudinal measurement of such cellular migration speeds *in vivo*. The potential speed of this migration is important because it represents a limiting factor for novel therapies based on mobilization of endogenous stem cells to peripheral sites. We also observed much slower migration rates as MPIO-cells distributed through the OB. While most MPIO-labeled cells differentiated into a neuronal phenotype, an increasing number of these particles were also located in phagocytic cell types, suggesting death of some of the originally labeled NB cells in the OB, which occurs under normal physiological conditions.

The rapid migration observed in the RMS likely represents an upper limit of the achievable migration rates in brain tissue. The RMS has a unique composition, defined by glial-sheathed chains of migrating NBs in close proximity to one another (Lois et al., 1996). The SVZ contains large networks of similar chains that permit the migration of cells along the ventricle walls and into the RMS (Doetsch and Alvarez-Buylla, 1996). Thus, throughout the SVZ and RMS and into the OB, there is an established cellular structure that facilitates NB migration. As cells begin exiting the RMS and dispersing through the OB, the speed of movement rapidly becomes slower. It is possible that migration through brain parenchyma, as a response to peripheral disease or injury for instance, would likewise be slower than rates observed in the RMS. In these cases, NBs must be coerced away from the normal route of established chain migration and move through alternative and less-traveled routes. In the future, a finer temporal sampling during RMS migration and OB distribution (Days 0 through 4) could provide more detailed measures of the migration rate extremes. These could then be compared with underlying cellular features (observed histologically) or with the distribution of chemoattractants or repellents to investigate their influence on the NB migration rate.

Recent results characterized the cell types of MPIO-labeled cells in the rat RMS and OB by magnetically and fluorescently activated cell sorting of large numbers of cells (Sumner et al., 2009). In comparison to those results, our immunohistological results show a larger number of migrating or immature neurons and fewer astrocytes (50% and 29% at Day 21 as compared to 10% and 40% in their OB data at Day 14). Although substantial differences in the counting methodologies cannot be ruled out as a source of discrepancy, it is also likely that mouse–rat species differences result in different cell type requirements. In addition, the anterior SVZ-targeted injections we describe here label only a subset of SVZ cells, in comparison to the larger ventricular injections used in their report which may result in labeling of a different sub-population of SVZ cells. On a similar note, in our own data, the BrdU labeling, which also labels cells throughout the SVZ, resulted in higher numbers of labeled cells than the MPIOs that were concentrated in only the anterior portion of the SVZ.

The surgical labeling of smaller portions of the SVZ as proposed here with MPIOs has differences, and some potential advantages over alternative methods. Recently, it has been shown that the NB population is organized spatially, such that various types of periglomerular and granule progenitor cells originate in segregated SVZ regions (Lledo et al., 2008; Merkle et al., 2007). As the separate subpopulations are not yet separable by immunohistochemical or genetic means, surgically targeted labeling may permit comparison of the relative migratory capacity of these different cell populations under normal and disease conditions. Furthermore, direct targeting of the SVZ permits use of relatively small volume MPIO-injections, resulting in a smaller artifact than comparable ventricular injections and thereby improving visualization near the injection site. In this study, this permitted quantification of migration over a large

region of the mouse RMS, an area apt to be obscured by large ventricular injections. It should also permit visualization of cells moving into the striatum or cortex, sites frequently obscured or distorted by large volume iron-oxide injections in the ventricle (Shapiro et al., 2006). Improvements in the efficiency of MPIO uptake by modification of the particles and a mapping of stereotaxic coordinates along the ventricle for improved targeting will further increase the potential applications of this labeling method.

Alternative methods of labeling and noninvasively imaging cells are an important topic of ongoing research. The use of genetic reporters is, of course, a very attractive possibility for mouse research that may ultimately provide a more powerful approach for long-term *in vivo* monitoring of specific cell populations. For studies in the mouse, where sub-millimeter accuracy is essential, image resolution must be kept very high. Optical methods, which have proven more easily adapted to genetic reporters, are limited in penetration and resolution and therefore difficult to apply in studies where spatially resolved dynamics are required deep within the brain. As a result, the development of an MR reporter gene continues to be an area of interest, despite the more limited sensitivity of MRI. Several potential candidates have been described, but the sensitivity of detecting relatively small numbers of labeled migrating cells has not been demonstrated (Cohen et al., 2005; Cohen et al., 2007; Deans et al., 2006; Genove et al., 2005; Gilad et al., 2007; Moore et al., 1998; Weissleder et al., 2000; Zurkiya et al., 2008). The imaging methods described here provide sufficient sensitivity, flexibility and spatial resolution to study SVZ-derived NB dynamics in normal and disease conditions, particularly where the migration or distribution of cellular populations needs to be monitored longitudinally.

This study has demonstrated quantitative measurement of rates and patterns of migration of neuronal precursors in the RMS and OB. The use of magnetically labeled cells and longitudinal MRI has enabled the first *in vivo* measurements of migration rates in the RMS, and suggests that precursor cells can travel very quickly under appropriate conditions. Similar measurements using MRI in conditions of disease or injury may reveal important factors affecting the ability of precursor cells to participate in tissue repair at novel sites throughout the brain or elsewhere in the CNS.

Acknowledgments

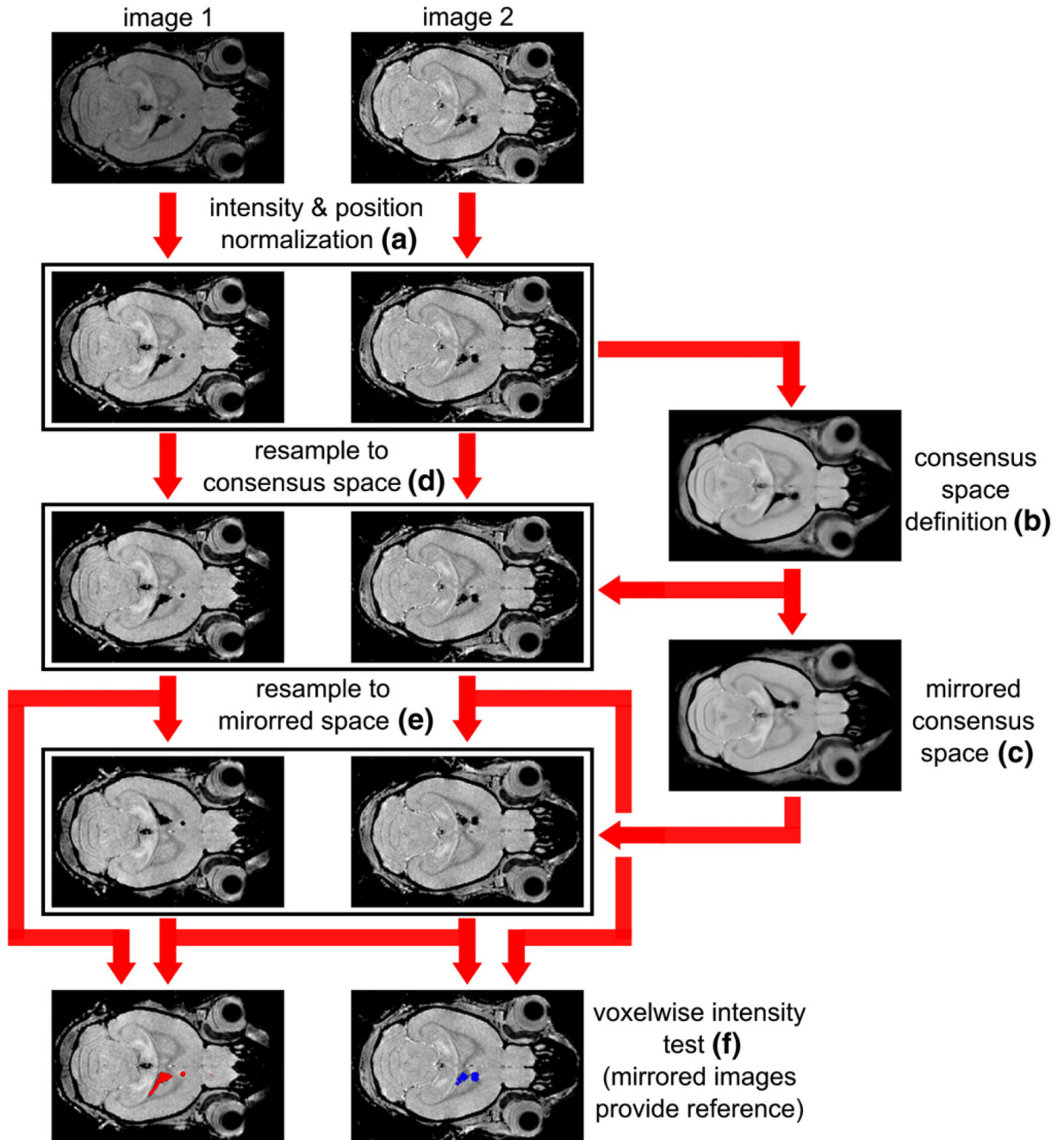
We thank Mark Henkelman, John Sled and Jason Lerch (Mouse Imaging Centre, Hospital for Sick Children, Toronto, Canada) for providing the software used for image registration. Funding for this work was provided by the New York State Department of Health, Spinal Cord Injury Research Board (contracts #C020926, C022053).

References

- Arvidsson A, Collin T, Kirik D, Kokaia Z, Lindvall O. Neuronal replacement from endogenous precursors in the adult brain after stroke. *Nat. Med* 2002;8:963–970. [PubMed: 12161747]
- Bayer SA, Yackel JW, Puri PS. Neurons in the rat dentate gyrus granular layer substantially increase during juvenile and adult life. *Science* 1982;216:890–892. [PubMed: 7079742]
- Benjamini Y, Hochberg Y. Controlling the false discovery rate—a practical and powerful approach to multiple testing. *J. R. Stat. Soc., Ser. B Methodol* 1995;57:289–300.
- Bolteus AJ, Bordey A. GABA release and uptake regulate neuronal precursor migration in the postnatal subventricular zone. *J. Neurosci* 2004;24:7623–7631. [PubMed: 15342728]
- Cohen B, Dafni H, Meir G, Harmelin A, Neeman M. Ferritin as an endogenous MRI reporter for noninvasive imaging of gene expression in C6 glioma tumors. *Neoplasia* 2005;7:109–117. [PubMed: 15802016]
- Cohen B, Ziv K, Plaks V, Israely T, Kalchenko V, Harmelin A, Benjamin LE, Neeman M. MRI detection of transcriptional regulation of gene expression in transgenic mice. *Nat. Med* 2007;13:498–503. [PubMed: 17351627]

- Collins DL, Neelin P, Peters TM, Evans AC. Automatic 3D intersubject registration of MR volumetric data in standardized Talairach space. *J. Comput. Assist. Tomogr* 1994;18:192–205. [PubMed: 8126267]
- Cooper O, Isacson O. Intrastratial transforming growth factor alpha delivery to a model of Parkinson's disease induces proliferation and migration of endogenous adult neural progenitor cells without differentiation into dopaminergic neurons. *J. Neurosci* 2004;24:8924–8931. [PubMed: 15483111]
- Corotto FS, Henegar JA, Maruniak JA. Neurogenesis persists in the subependymal layer of the adult mouse brain. *Neurosci. Lett* 1993;149:111–114. [PubMed: 8474679]
- Deans AE, Wadghiri YZ, Bernas LM, Yu X, Rutt BK, Turnbull DH. Cellular MRI contrast via coexpression of transferrin receptor and ferritin. *Magn. Reson. Med* 2006;56:51–59. [PubMed: 16724301]
- Doetsch F, Alvarez-Buylla A. Network of tangential pathways for neuronal migration in adult mammalian brain. *Proc. Natl. Acad. Sci. U. S. A* 1996;93:14895–14900. [PubMed: 8962152]
- Fallon J, Reid S, Kinyamu R, Opole I, Opole R, Baratta J, Korc M, Endo TL, Duong A, Nguyen G, Karkehabadhi M, Twardzik D, Patel S, Loughlin S. In vivo induction of massive proliferation, directed migration, and differentiation of neural cells in the adult mammalian brain. *Proc. Natl. Acad. Sci. U. S. A* 2000;97:14686–14691. [PubMed: 11121069]
- Genove G, DeMarco U, Xu H, Goins WF, Ahrens ET. A new transgene reporter for in vivo magnetic resonance imaging. *Nat. Med* 2005;11:450–454. [PubMed: 15778721]
- Gilad AA, McMahon MT, Walczak P, Winnard PT Jr, Raman V, van Laarhoven HW, Skoglund CM, Bulte JW, van Zijl PC. Artificial reporter gene providing MRI contrast based on proton exchange. *Nat. Biotechnol* 2007;25:217–219. [PubMed: 17259977]
- Hirota Y, Ohshima T, Kaneko N, Ikeda M, Iwasato T, Kulkarni AB, Mikoshiba K, Okano H, Sawamoto K. Cyclin-dependent kinase 5 is required for control of neuroblast migration in the postnatal subventricular zone. *J. Neurosci* 2007;27:12829–12838. [PubMed: 18032654]
- Kolb B, Morshead C, Gonzalez C, Kim M, Gregg C, Shingo T, Weiss S. Growth factor-stimulated generation of new cortical tissue and functional recovery after stroke damage to the motor cortex of rats. *J. Cereb. Blood Flow Metab* 2007;27:983–997. [PubMed: 16985505]
- Kovacevic N, Henderson JT, Chan E, Lifshitz N, Bishop J, Evans AC, Henkelman RM, Chen XJ. A three-dimensional MRI atlas of the mouse brain with estimates of the average and variability. *Cereb. Cortex* 2005;15:639–645. [PubMed: 15342433]
- Lerch JP, Carroll JB, Spring S, Bertram LN, Schwab C, Hayden MR, Henkelman RM. Automated deformation analysis in the YAC128 Huntington disease mouse model. *Neuroimage* 2008;39:32–39. [PubMed: 17942324]
- Lledo PM, Merkle FT, Alvarez-Buylla A. Origin and function of olfactory bulb interneuron diversity. *Trends Neurosci* 2008;31:392–400. [PubMed: 18603310]
- Lois C, Alvarez-Buylla A. Long-distance neuronal migration in the adult mammalian brain. *Science* 1994;264:1145–1148. [PubMed: 8178174]
- Lois C, Garcia-Verdugo JM, Alvarez-Buylla A. Chain migration of neuronal precursors. *Science* 1996;271:978–981. [PubMed: 8584933]
- Luskin MB, Boone MS. Rate and pattern of migration of lineally-related olfactory bulb interneurons generated postnatally in the subventricular zone of the rat. *Chem. Senses* 1994;19:695–714. [PubMed: 7735848]
- Merkle FT, Mirzadeh Z, Alvarez-Buylla A. Mosaic organization of neural stem cells in the adult brain. *Science* 2007;317:381–384. [PubMed: 17615304]
- Moore A, Basilion JP, Chioccia EA, Weissleder R. Measuring transferrin receptor gene expression by NMR imaging. *Biochim. Biophys. Acta* 1998;1402:239–249. [PubMed: 9606982]
- Nait-Oumesmar B, Decker L, Lachapelle F, Avellana-Adalid V, Bachelin C, Van Evercooren AB. Progenitor cells of the adult mouse subventricular zone proliferate, migrate and differentiate into oligodendrocytes after demyelination. *Eur. J. Neurosci* 1999;11:4357–4366. [PubMed: 10594662]
- Nieman BJ, Flenniken AM, Adamson SL, Henkelman RM, Sled JG. Anatomical phenotyping in the brain and skull of a mutant mouse by magnetic resonance imaging and computed tomography. *Physiol. Genomics* 2006;24:154–162. [PubMed: 16410543]

- Nieman BJ, Szulc KU, Turnbull DH. Three-dimensional, in vivo MRI with selfgating and image coregistration in the mouse. *Magn. Reson. Med* 2009;61:1148–1157. [PubMed: 19253389]
- Shapiro EM, Gonzalez-Perez O, Manuel Garcia-Verdugo J, Alvarez-Buylla A, Koretsky AP. Magnetic resonance imaging of the migration of neuronal precursors generated in the adult rodent brain. *Neuroimage* 2006;32:1150–1157. [PubMed: 16814567]
- Sled JG, Zijdenbos AP, Evans AC. A nonparametric method for automatic correction of intensity nonuniformity in MRI data. *IEEE Trans. Med. Imaging* 1998;17:87–97. [PubMed: 9617910]
- Sumner JP, Shapiro EM, Maric D, Conroy R, Koretsky AP. In vivo labeling of adult neural progenitors for MRI with micron sized particles of iron oxide: quantification of labeled cell phenotype. *Neuroimage* 2009;44:671–678. [PubMed: 18722534]
- Tattersfield AS, Croon RJ, Liu YW, Kells AP, Faull RL, Connor B. Neurogenesis in the striatum of the quinolinic acid lesion model of Huntington's disease. *Neuroscience* 2004;127:319–332. [PubMed: 15262322]
- Thored P, Arvidsson A, Cacci E, Ahlenius H, Kallur T, Darsalia V, Ekdahl CT, Kokaia Z, Lindvall O. Persistent production of neurons from adult brain stem cells during recovery after stroke. *Stem Cells* 2006;24:739–747. [PubMed: 16210404]
- Weissleder R, Moore A, Mahmood U, Bhorade R, Benveniste H, Chiocca EA, Basilion JP. In vivo magnetic resonance imaging of transgene expression. *Nat. Med* 2000;6:351–355. [PubMed: 10700241]
- Wichterle H, Garcia-Verdugo JM, Alvarez-Buylla A. Direct evidence for homotypic, glia-independent neuronal migration. *Neuron* 1997;18:779–791. [PubMed: 9182802]
- Woods RP, Grafton ST, Holmes CJ, Cherry SR, Mazziotta JC. Automated image registration: I. General methods and intrasubject, intramodality validation. *J. Comput. Assist. Tomogr* 1998a;22:139–152. [PubMed: 9448779]
- Woods RP, Grafton ST, Watson JD, Sicotte NL, Mazziotta JC. Automated image registration: II. Intersubject validation of linear and nonlinear models. *J. Comput. Assist. Tomogr* 1998b;22:153–165. [PubMed: 9448780]
- Zurkiya O, Chan AW, Hu X. MagA is sufficient for producing magnetic nanoparticles in mammalian cells, making it an MRI reporter. *Magn. Reson. Med* 2008;59:1225–1231. [PubMed: 18506784]

**Fig. 1.**

Intensity-based analyses of labeled MR images. To isolate hypointense, labeled voxels in MR images, images were first aligned to a reference (removing translation and rotation differences) and intensity-normalized (a). The set of all images—only two are shown for simplicity—was used to define a consensus space (b), unbiased toward any individual image. An average in the consensus space was mirrored left-to-right and registered upon itself (c) to define a mirrored space. Images were resampled into each of these spaces (d and e) so that all image voxels were aligned. Intensity values of individual voxel in each image were then tested against the corresponding values in the contralateral voxel, using a color overlay to indicate voxels with

significant differences in intensity (f; red in left panel, blue in right panel). The entire set of images was used to characterize the expected unlabeled signal-intensity distribution.

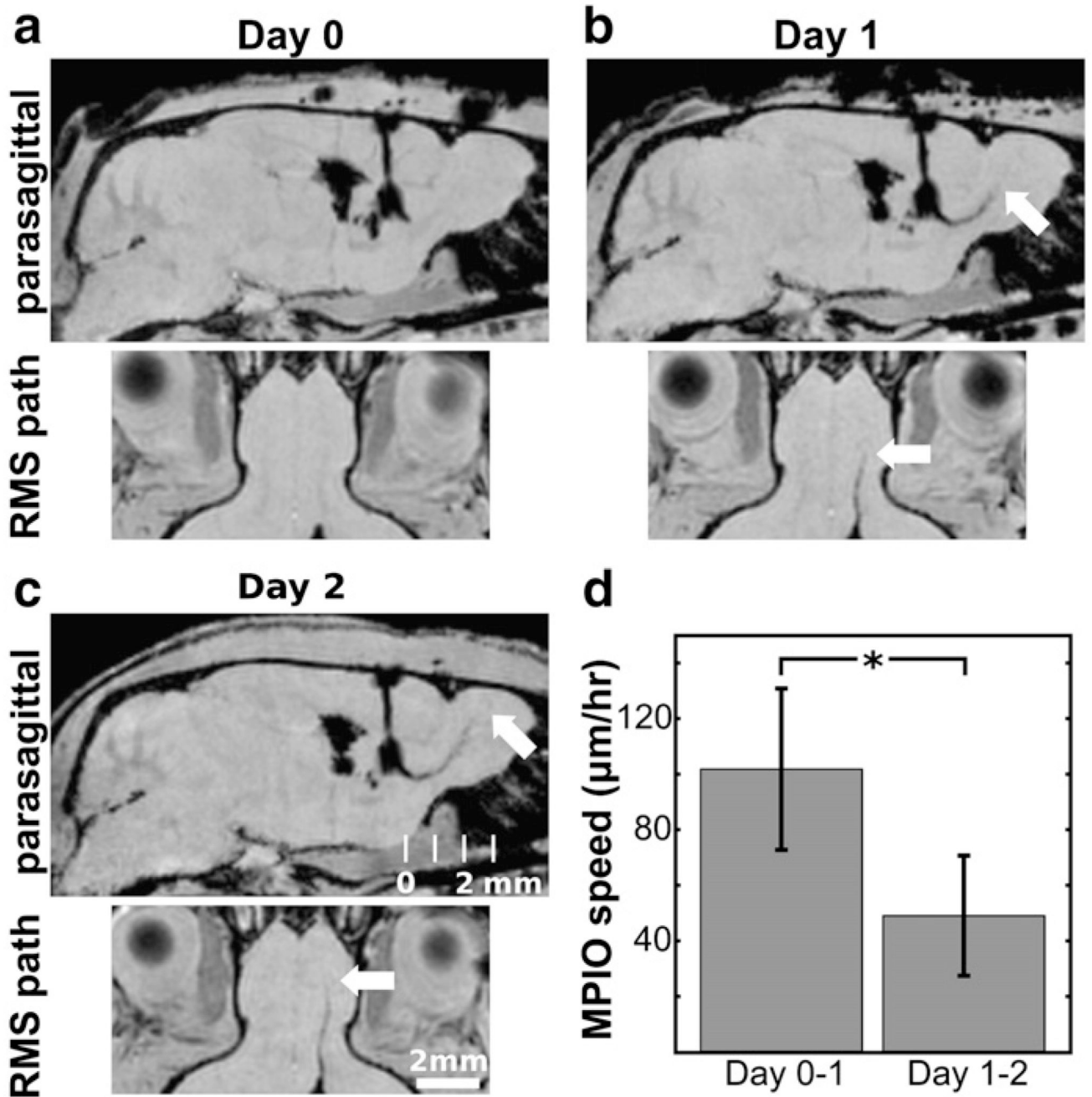


Fig. 2. Migration rate in the RMS. Hypointensities in the vicinity of the RMS were observed shortly after surgical injection of MPIOs. Images from an individual mouse are shown on Days 0 (a), 1 (b) and 2 (c) after injection. A hypointense line (white arrows, b and c) marked the progression of the MPIOs in both the parasagittal plane (upper panels, a–c), and a plane reformatted to run along the RMS perpendicular to the parasagittal plane (lower panels, a–c). Measurement of the distance of progression between days provided an estimate of the speed of migration of MPIOs. Speed averages ($N = 4$ mice) for Days 0–1 and Days 1–2 are shown in panel d, where error bars represent the standard deviation. The speed on Days 1–2 in the caudal region of the OB was significantly slower than the speed on Days 0–1 in the RMS ($*p < 0.05$).

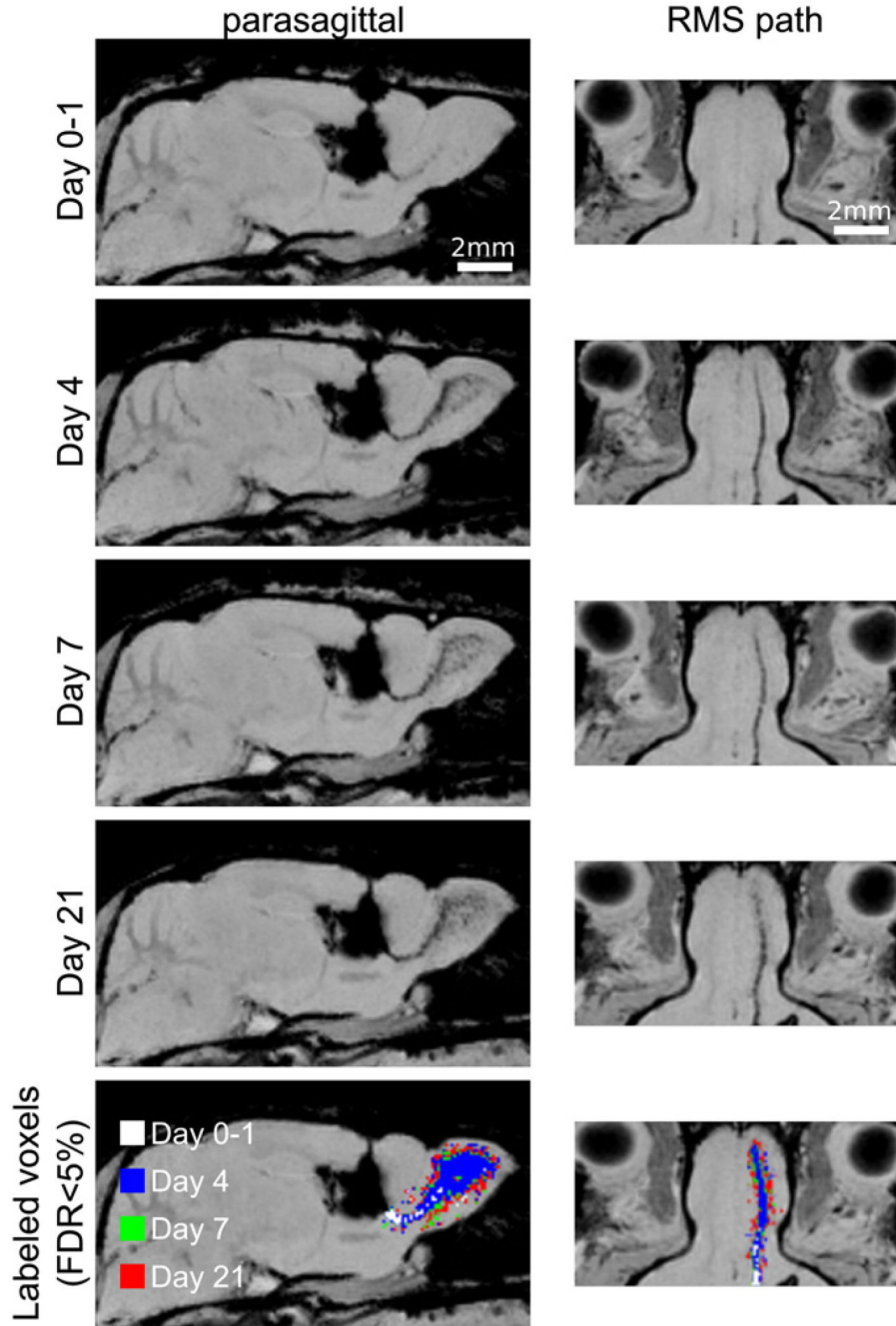


Fig. 3. Distribution of MPIO in the olfactory bulb. Parasagittal and RMS reformatted images are shown at Days 0–1 (combining images from 3 to 24 h post-injection), Day 4, Day 7 and Day 21. Each image is representative of a composite of three or more individual animals. Distribution through the bulb occurs primarily in the parasagittal plane (left column) with relatively little motion laterally (as seen in the right column). In the lowest row of images, a color overlay indicates voxels determined to be significantly hypointense ($FDR < 0.05$) for each day. Earlier days are shown superimposed on later ones. Slow migration into the OB was evident by the limited green and red rim (Days 7 and 21, respectively) extending beyond the

blue Day 4 region. In contrast, significant changes were evident between Days 0–1 and 4 (white and blue, respectively).

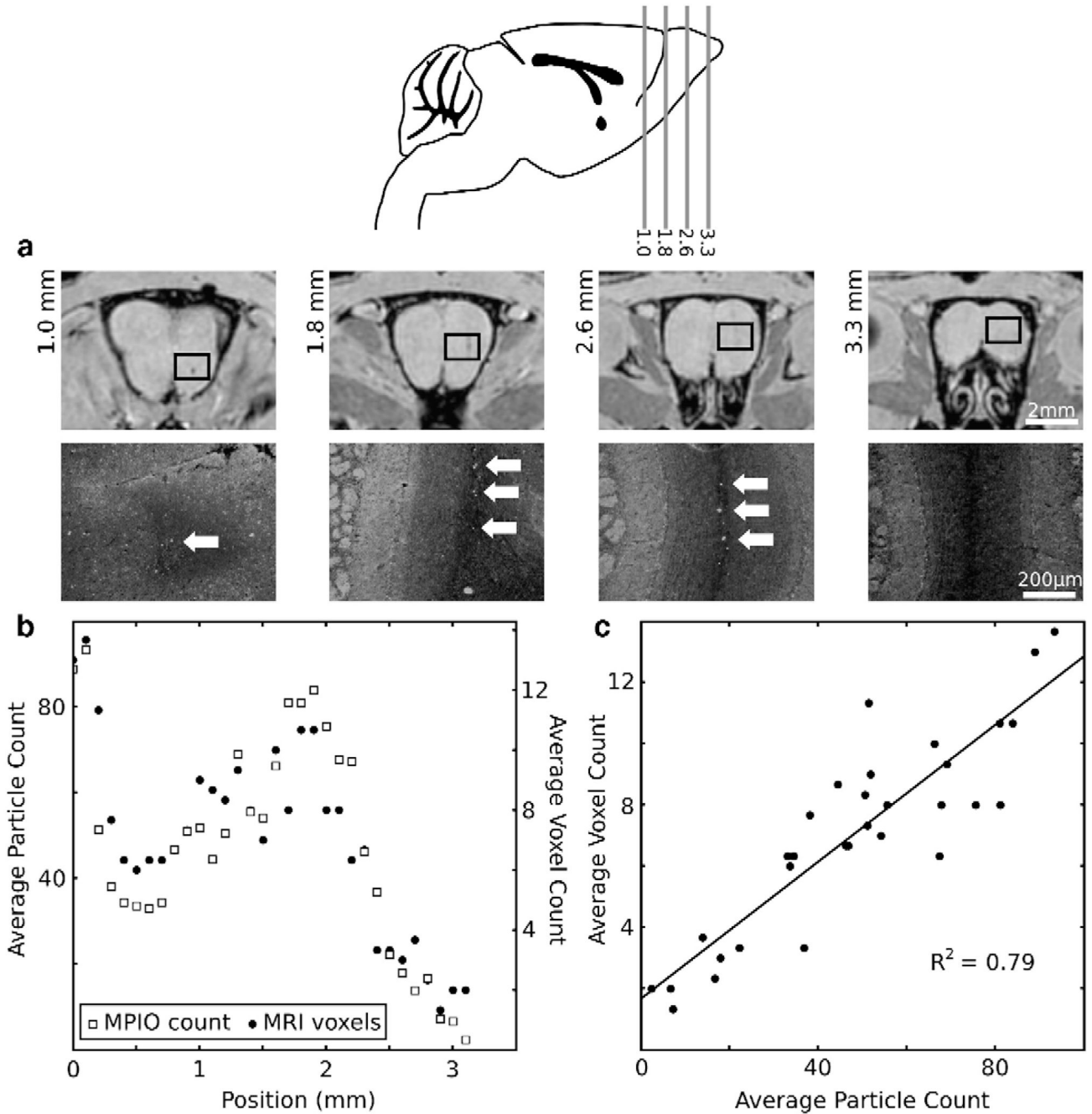


Fig. 4. Comparative analyses of MRI and histological MPIO distribution. (a) The hypointense regions in MR images (upper panels) qualitatively matched the distribution of particles observed on histological sections (lower panels). MPIOs were easily detected as bright particles (arrows) on a dim autofluorescent background. The image histogram has been modified to show the particles here in an anatomical context. The location of each (lower) histological image is shown on the corresponding (upper) MR image with a box. The location (in mm) for each MR image is indicated on the sagittal schematic (inset). (b) Average measurements ($N=3$ mice) show the quantitative correspondence between histology particle count (left axis) and MRI voxel count (right axis) as a function of anterior-posterior position along the RMS/OB. (c)

Plotting the voxel count as a function of the particle count for each position showed a highly correlated, linear relationship between the two ($R^2 = 0.79$).

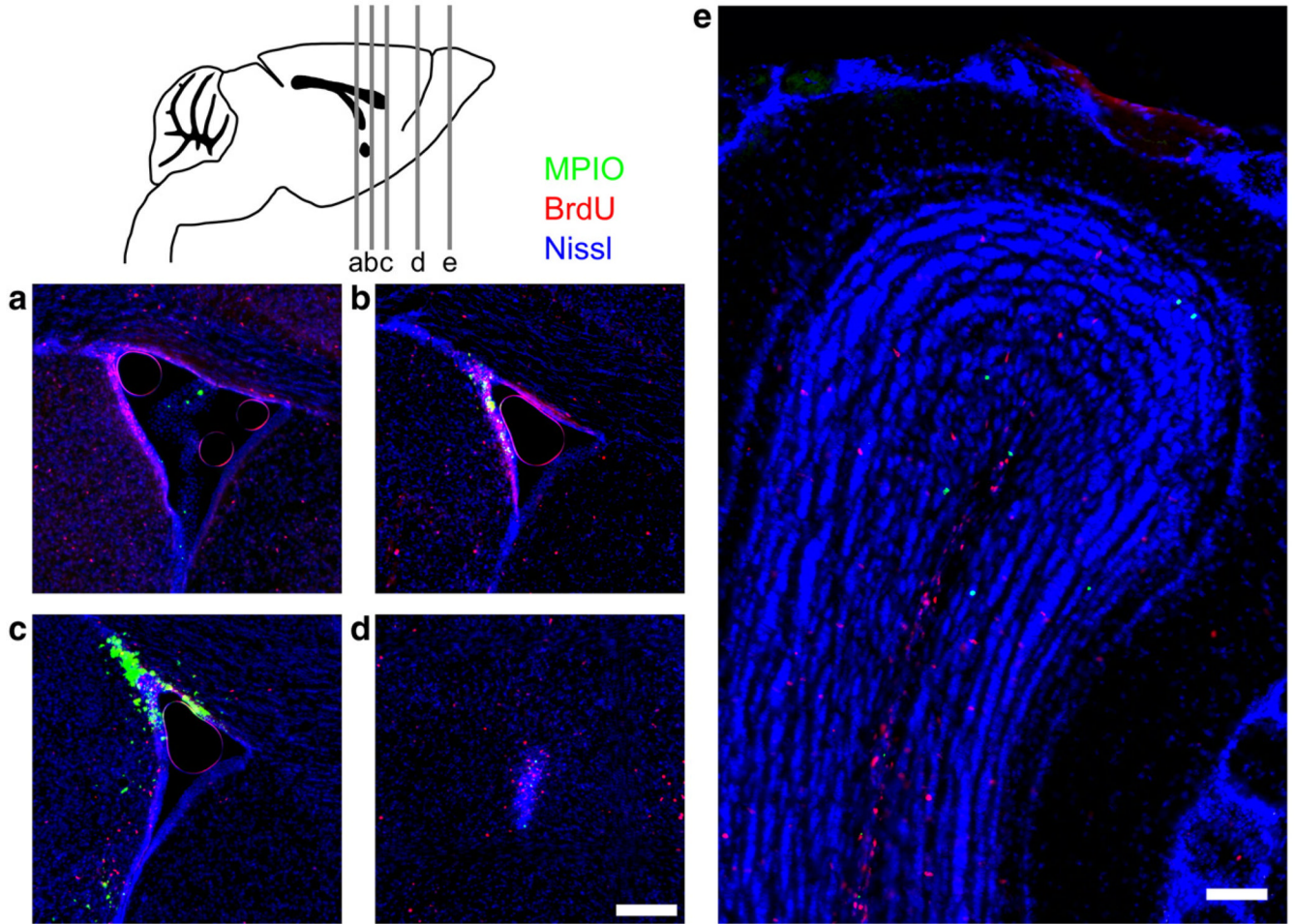


Fig. 5. Histological visualization of post-injection particles. The MPIO injection resulted in significant accumulation of particles in the anterior region of the SVZ. Panels here show results at Day 7 post-injection. Green shows the Dragon Green fluorescence of the encapsulated MPIOs, red shows BrdU and blue shows a Nissl stain. More caudal portions of the SVZ (a) did not show significant accumulation of particles even when isolated particles were evident in the ventricles. Advancing to the rostral portion of the SVZ (b, c) showed more notable accumulation of MPIOs in the SVZ. In the RMS (d) and OB (e), MPIOs were observed in a spatial distribution similar to BrdU positive cells, but colocalization of the MPIO and BrdU was not generally observed. A sagittal schematic (top left) shows the approximate locations of each section from left to right (a to e, respectively). Scale bars in panels d (for a–d) and e represent 100 μ m.

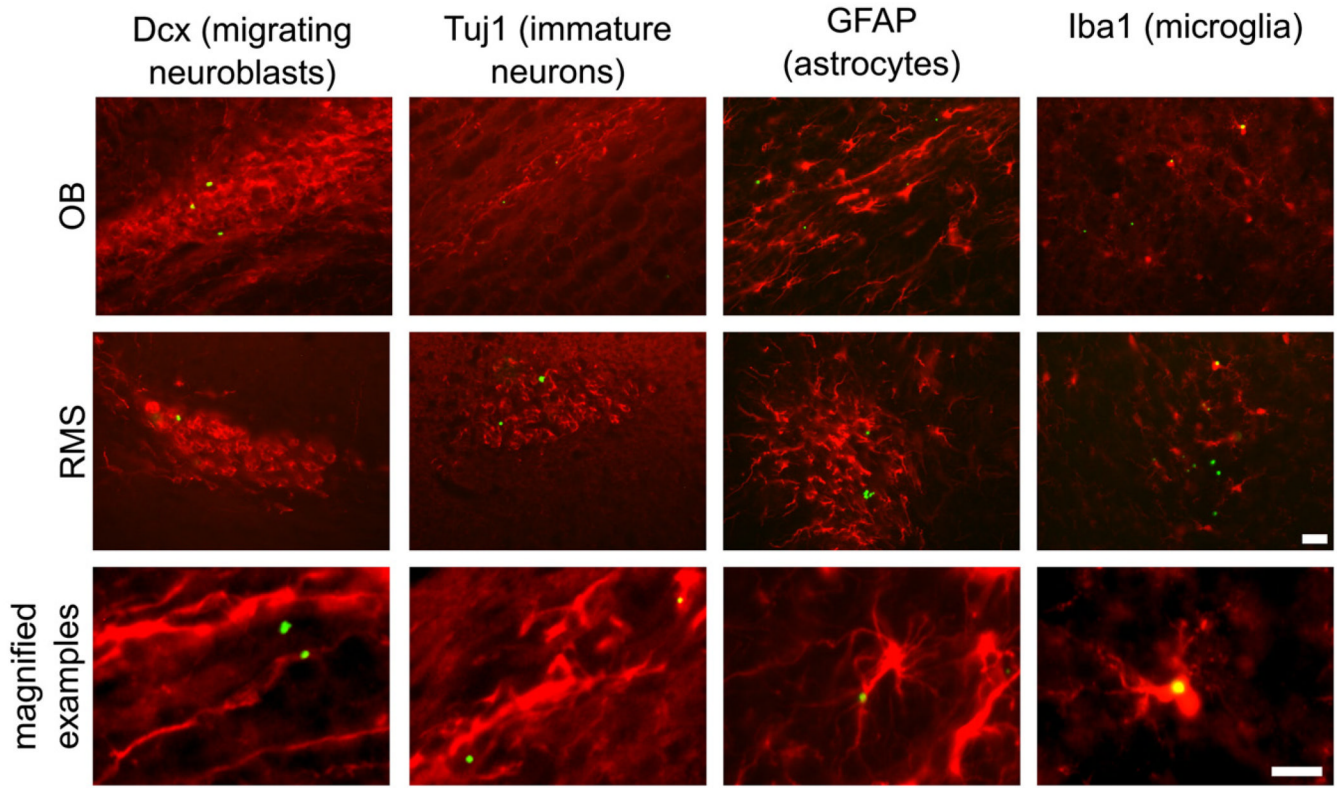


Fig. 6. Immunohistochemistry of MPIO-labeled cells. Sample histological sections are provided for each of the markers assayed. Sections were stained for Dcx, Tuj1, GFAP and Iba1. Examples are shown for each stain from the OB (top panels), the RMS (middle panels), as well as a higher magnification image for each cell type (bottom). Scale bars represent 20 (for all OB and RMS images) and 10 μm (for all magnified examples) in the lower panels.

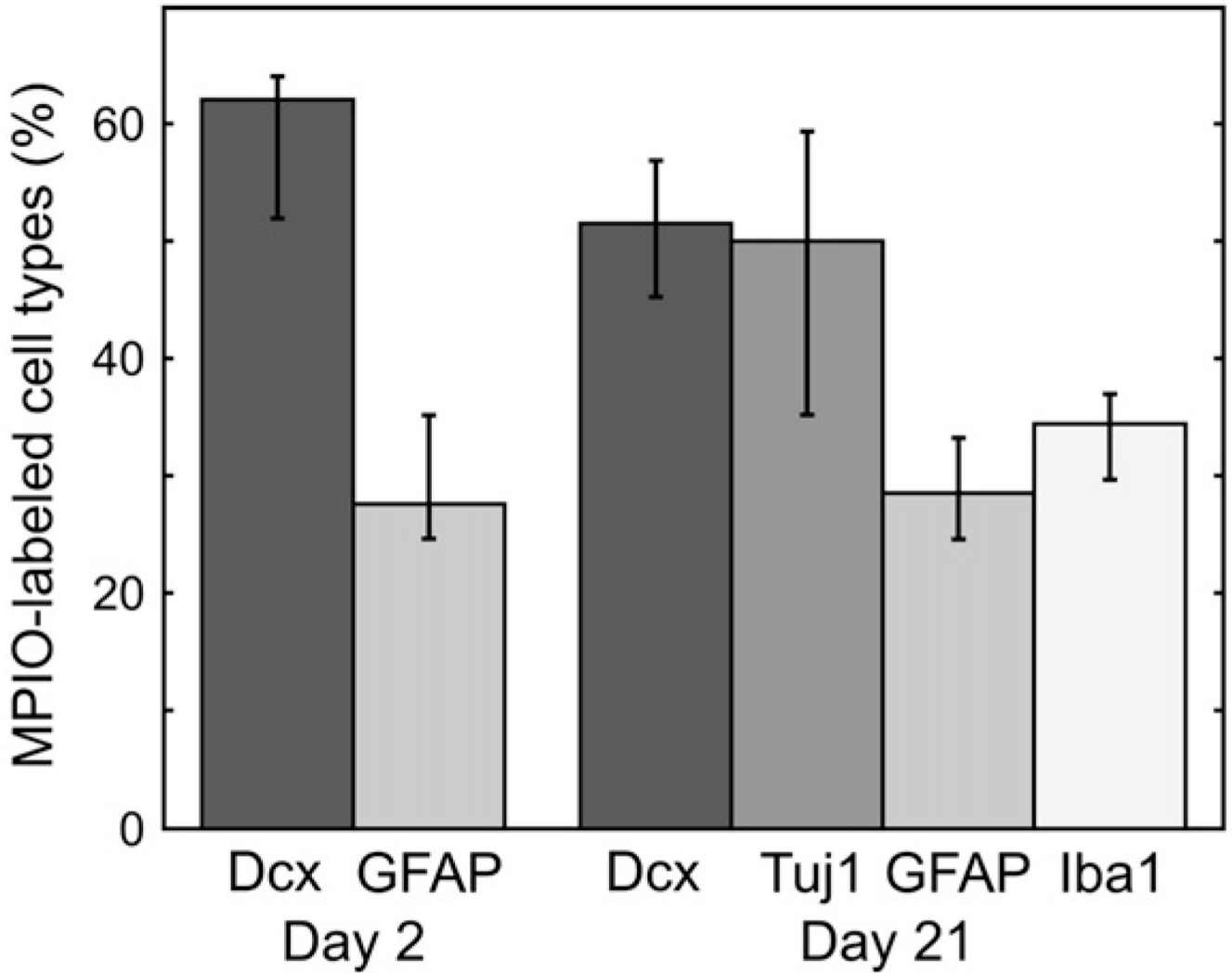


Fig. 7.

Quantitative analysis of MPIO-labeled cell types. Three readers scored all sections (examples shown in Fig. 6) to determine the types of cells labeled by the MPIO injection on Days 2 and 21. The bar graph shows the reader consensus percentage of MPIO-labeled cells and the error bars show the full range of percentages assigned by individual readers. Note that Dcx and Tuj1 are expected to show a high degree of overlap in these analyses.